

Thermometry of plasmonic nanostructures by anti-Stokes electronic Raman scattering

Xu Xie, and David G. Cahill

Citation: [Appl. Phys. Lett.](#) **109**, 183104 (2016);

View online: <https://doi.org/10.1063/1.4966289>

View Table of Contents: <http://aip.scitation.org/toc/apl/109/18>

Published by the [American Institute of Physics](#)

Articles you may be interested in

[Nanoscale thermal transport](#)

[Journal of Applied Physics](#) **93**, 793 (2002); 10.1063/1.1524305

[Effects of basal-plane thermal conductivity and interface thermal conductance on the hot spot temperature in graphene electronic devices](#)

[Applied Physics Letters](#) **110**, 073104 (2017); 10.1063/1.4976511

[Nanoscale thermometry by scanning thermal microscopy](#)

[Review of Scientific Instruments](#) **87**, 074902 (2016); 10.1063/1.4955449

[Analysis of heat flow in layered structures for time-domain thermoreflectance](#)

[Review of Scientific Instruments](#) **75**, 5119 (2004); 10.1063/1.1819431

[An anisotropic model for the minimum thermal conductivity](#)

[Applied Physics Letters](#) **107**, 193104 (2015); 10.1063/1.4935467

[Fine-tuning the metallic core-shell nanostructures for plasmonic perovskite solar cells](#)

[Applied Physics Letters](#) **109**, 183901 (2016); 10.1063/1.4966893



SciLight

Sharp, quick summaries **illuminating**
the latest physics research

Sign up for **FREE!**

AIP
Publishing

Thermometry of plasmonic nanostructures by anti-Stokes electronic Raman scattering

Xu Xie^{a)} and David G. Cahill^{a)}

Department of Materials Science and Engineering, Materials Research Laboratory, University of Illinois at Urbana-Champaign, Urbana, Illinois 61801, USA

(Received 7 August 2016; accepted 16 October 2016; published online 31 October 2016)

Measurements of temperature of optically excited plasmonic nanostructures are needed to evaluate their functionality and thermal stability. Here, we describe a simple, accurate, and non-invasive thermometry based on anti-Stokes electronic Raman scattering. We validate the approach using an array of uniformly heated Au nanodisks and perform experiments on the heating of individual nanodisk by a focused laser beam. The steady-state temperature rise of an individual nanodisk has comparable contributions from the thermal conductance of the Au/quartz interface and heat spreading in the quartz substrate. The temperature measurements have an accuracy of 3% of the absolute temperature in the range of temperatures $300 < T < 700$ K. *Published by AIP Publishing.*
[\[http://dx.doi.org/10.1063/1.4966289\]](http://dx.doi.org/10.1063/1.4966289)

Recent advances in plasmonics are enabling new applications^{1,2} in chemical sensing,^{3,4} bio-imaging,^{5,6} photothermal therapy,^{7,8} light harvesting,^{9,10} and heat-assisted magnetic recording (HAMR).^{11,12} Heating of plasmonic structures due to the interaction with light is a critical parameter for the performance (e.g., stability and efficiency) and engineering design of plasmonic structures.^{2,12} Such heating is of particular concern in HAMR, an emerging data-storage technology that enables storage densities surpassing 1 TB in⁻².^{13,14} In HAMR, a near-field optical transducer (NFT) (essentially a Au plasmonic nanodisk with a peg^{11,15}) focuses near infrared light in the near field to heat a sub-25 nm region of magnetic recording media.¹² Transient heating of the media enables the use of recording materials with extremely high coercive fields that are immune to the loss of information from thermal-fluctuations at ambient temperature. Unfortunately, the NFT itself is also significantly heated by the excitation laser, which can lead to undesirable changes in the microstructure and shape of the NFT. Measurement of the NFT operating temperature (up to $\approx 400^\circ\text{C}$ (Ref. 15)) is needed to improve the thermal management of the recording device.¹²

Thermometry based on scanning probe microscopy, such as scanning thermal microscopy (SThM)¹⁶ and scanning Joule expansion microscopy (SJEM),¹⁷ has the capability of characterizing temperature excursions with sub-100 nm spatial resolution. SThM and SJEM, however, disturb the local distribution of electromagnetic fields and temperature in a plasmonic structure. Many forms of far-field spectroscopies have been used to determine temperatures: e.g., refractive index variation,¹⁸ fluorescence intensity,¹⁹ lifetime,²⁰ and polarization anisotropy;²¹ and vibrational Raman intensity²² and peak shifts.²³ However, these methods typically rely on the response of neighboring materials or coatings, which require additional calibration, suffer from instability, and fail to directly access the temperature of the plasmonic metal nanostructure. At nanometer length scales,

the thermal resistance of interfaces can produce a significant temperature drop between the source of heat and the surroundings.²⁴

Here, we introduce a non-invasive, quantitative thermometry based on anti-Stokes inelastic light scattering that directly probes the temperature of plasmonic nanostructures. Inelastically scattered light from metallic plasmonic structures presents as a broad spectral continuum.²⁵ Recently, Huang *et al.* discovered that the intensity of inelastic light scattered from the suspension of Au nanorods excited by a pulsed laser can be quantitatively connected to the electronic temperature²⁶ using a description based on “electronic Raman scattering” by a thermal distribution of electronic excitations. Subsequent studies observed similar temperature-dependence and extended this description of inelastically scattered light to various plasmonic structures, e.g., inverted Au pyramids,²⁷ Au nanocrystals on Si substrate,²⁸ and Ag nanocrystals embedded in SiO₂.^{29,30}

In this work, we extend this approach to the level of an individual Au nanodisk and demonstrate that anti-Stokes Raman scattering can serve as a practical tool for *in-situ* measurement of the temperature of individual and arrays of plasmonic structures.

We first validated our approach with plasmonic structures that are uniformly heated by a heating stage. The sample consists of Au nanodisks patterned on a crystalline quartz substrate (see the inset of Fig. 1(a)) via “hole-mask colloidal lithography.”³¹ Details of the fabrication process appear in Fig. S1 in the [supplementary material](#).

We spectrally tuned the plasmon resonance close to 785 nm (the wavelength of the laser for optical excitation) by adjusting the diameter D , height h , and the dielectric environment of the nanodisks (Fig. 1(a) and Fig. S2 in the [supplementary material](#)). We found that the shape of the Au nanodisks was unstable at elevated temperatures. Adding a thin dielectric capping layer (typically 30 nm SiO₂ via e-beam evaporation) followed by annealing (≈ 15 min) stabilizes the nanodisks at temperatures below the annealing temperature (Fig. S3 in the [supplementary material](#)). The

^{a)}Authors to whom correspondence should be addressed. Electronic addresses: xuxie1@illinois.edu and d-cahill@illinois.edu

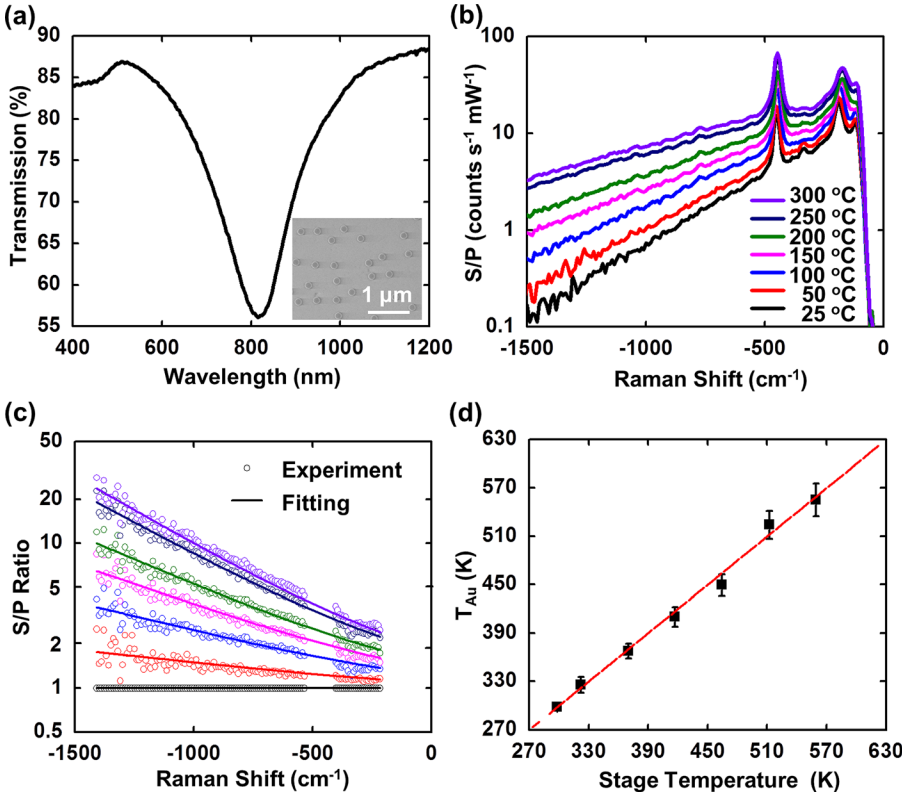


FIG. 1. (a) Optical transmission spectrum of an array of plasmonic nanodisks supported on a double-side-polished crystalline quartz substrate. The inset shows the scanning electron microscopy (SEM) image of the array. (b) Anti-Stokes electronic Raman scattering spectra collected from arrays of nanodisks as a function of substrate temperature. The y-axis is the spectral density of the intensity S of scattered light (i.e., the counts reported by the CCD camera per second) normalized by the excitation laser power P . (c) Raman spectra for different heating temperatures normalized by the spectrum collected at 25 °C (i.e., the baseline spectrum). The circles are experimental data from (b), and the lines are fitting results with the temperature of nanodisks as the only variable. (d) Comparison between the temperature extracted from the fit in (c) and the temperature of the heating stage. Dashed red line with a slope of 1 is for reference.

full-width-at-half-maximum (FWHM ≈ 190 nm) of the extinction peak (Fig. 1(a)) is larger than the estimation (FWHM ≈ 110 nm) based on the spheroid model,^{32,33} likely due to the polydispersity of the diameters of the nanodisks.

The laser we use to excite Raman scattering is a Ti:sapphire oscillator operated in the continuous wave (CW) mode with the wavelength tuned to 785 ± 1 nm. A $10\times$ objective lens focuses the 5 mW beam to a $1/e^2$ intensity radius W_0 of $\approx 5.1 \mu\text{m}$. The relatively large spot size and intermediate laser power provide adequate signal strength and negligible laser heating. The temperature rise due to laser heating can be estimated as $\Delta T = \frac{P_{\text{abs}}}{2\sqrt{\pi}W_0\Lambda} \approx 3$ K, where P_{abs} is the absorbed laser power and Λ is the thermal conductivity of the quartz substrate. Two high-pass spectra filters remove elastically scattered light before the inelastically scattered light enters the spectrometer.

We utilize the anti-Stokes Raman scattering rather than the Stokes Raman scattering for the thermometry, due to the stronger dependence of the intensity on the temperature for the anti-Stokes Raman scattering (Fig. S4 of the [supplementary material](#)).

Figure 1(b) shows a series of spectra for an ensemble of nanodisks (diameter ≈ 174 nm and density ≈ 3.3 nanodisks μm^{-2}) with temperatures controlled by a heating stage. The y-axis is the signal S recorded by the CCD detector normalized by the laser power (P) and integration time (typically 200 s); the x-axis is the wavenumber shift with respect to 785 nm. The Raman intensity decreases exponentially with decreasing wave-number, and increases with increasing temperature. Vibrational peaks of the substrate appear at 207 cm^{-1} and 467 cm^{-1} .³⁴

We attribute the spectra of inelastically scattered light to Raman scattering by a thermal distribution of electron-hole

pairs in Au. Momentum conservation is relaxed due to the small size of the Au nanodisks, and the plasmonic resonance enhances both absorption and scattering cross-sections. Under this picture, the spectral intensity $S(\Delta\omega)$ (Raman signals per unit integrating time) scales with the electron-hole occupation number

$$n(\Delta\omega) = \frac{1}{\exp(-hc\Delta\omega/k_B T_{\text{Au}}) - 1}, \quad (1)$$

where h is Planck's constant, c is the speed of light, $\Delta\omega$ is the wavenumber (negative for anti-Stokes), and T_{Au} is the temperature of the Au nanodisk.

We utilize the temperature-dependent and wavelength-dependent intensity of scattered light for extracting T_{Au} . We do not expect $S(\Delta\omega)$ simply follows a scaling factor times $n(\Delta\omega)$ due to the dependence of the Raman enhancement factor and Raman cross-section on wavelength.³⁵ We first divided the spectral intensity at each temperature $S(\Delta\omega)_{\text{Au}}$ by a baseline $S(\Delta\omega)_0$, i.e., the intensity of spectrum taken at $T_0 = 298$ K

$$\frac{S(\Delta\omega)_{\text{Au}}}{S(\Delta\omega)_0} = \frac{\exp(-hc\Delta\omega/k_B T_0) - 1}{\exp(-hc\Delta\omega/k_B T_{\text{Au}}) - 1}. \quad (2)$$

Normalization of the data in this way simplifies the data analysis by removing the wavelength dependence of the Raman cross-sections, Raman enhancement factors, transmission of optical path, and the efficiency of grating and detector.

The circles in Fig. 1(c) are experimental data of the ratio $\frac{S(\Delta\omega)_{\text{Au}}}{S(\Delta\omega)_0}$. As the wavenumber decreases, the ratio increases as

expected from Eq. (2). The noise is larger than that of the data before normalization (Fig. 1(b)) due to the propagation of noise from the baseline. We fit the ratio using Eq. (2) with T_{Au} as the only fitting parameter (lines in Fig. 1(c)). The spectral regions of quartz Raman signals (i.e., the data appearing at around 207 cm^{-1} and 467 cm^{-1}) are excluded because they do not follow the same occupation (Eq. (1)) due to the broadening of the vibrational peaks as the temperature rises and the possible changes of the Raman cross-sections.³⁶ We discuss sensitivities, noise, and uncertainties for these fits in Fig. S4 of the [supplementary material](#). Good fits in Fig. 1(c) reveal that Eq. (2) describes the data sets well.

Figure 1(d) shows the temperatures extracted from the fits of the data using Eq. (2) in comparison to the temperature of the heating stage. The good agreement validates the approach based on Eq. (2). We emphasize that the baseline can be readily collected from the Raman setup at room temperature. Once the single set of baseline spectrum is collected, the data reduction does not require extra calibration. The changes in intensity relatively to the baseline are determined by a simple Bose-Einstein factor. The error bars in Fig. 1(d) are calculated based on the goodness-of-fit between Eq. (2) and the datasets. We define σ_{min} as the minimal sum of squared residues between the ratio data and fitting.³⁷ The upper and lower values of T_{Au} that result in a sum of squared residues equal to $2\sigma_{\text{min}}$ constitute the bounds of uncertainties in T_{Au} (corresponding to a 95% confidence interval). The error bars increase as the temperature rises, due to the reduction of sensitivity in fitting. The accuracy of the thermometry on arrays of plasmonic nanodisks is $\approx 2\%$.

To study the thermometry at the level of an individual nanodisk, we prepared Au nanodisks dispersed sparsely on the substrate, with spacing between a nanodisk and nearest neighbor of $\approx 1.2\text{ }\mu\text{m}$ (Fig. 2(a)). Covering the sample with

30 nm SiO_2 followed by annealing at 350°C improves the thermal stability. The wavelength of plasmonic resonance was adjusted to 790 nm (Fig. S5 in the [supplementary material](#)). An objective lens of $50\times$ focuses the laser beam onto the sample with a $1/e^2$ radius of $\approx 1.1\text{ }\mu\text{m}$. We aligned individual nanodisks in the center of the laser beam by maximizing the Raman intensity under a large power illumination (30 mW).

Figure 2(b) shows a series of spectra collected from a representative nanodisk as a function of laser power. The baseline at 5 mW is noisy, due to the small probing power. At higher laser power, the Raman intensity and the signal-to-noise (S/N) ratio increase. Overall, the spectral intensity is small compared to that from the sample with high nanodisk density. As a result, the contribution of the background signals (e.g., fluorescence from the quartz substrate, objective lens, and other optics, see Fig. S6 in the [supplementary material](#)), is significant. The background, shown as the green curve in Fig. 2(b), was collected at a region on the quartz substrate without any nanodisks.

We did not observe apparent drifts of the spectral intensity during the measurements. The change of Raman intensity based on monitoring the same nanodisk (during 15 min) is smaller than 5%. This variation adds a systematic error of about 1% to the extracted temperature.

The extraction of nanodisk temperature uses similar analysis described in the above paragraph. The background signal is first subtracted from each spectrum. To reduce the propagation of noise from the baseline (i.e., the spectrum collected at a laser power of 5 mW), we averaged the adjacent 5 points in the data for smoothing. Figure 2(c) shows the normalized spectral intensity and fits based on Eq. (2) using T_{Au} as the single free parameter. Since the temperature of the baseline T_0 is unknown (heating at 5 mW is non-negligible), we fit the spectra for different laser powers to reach a

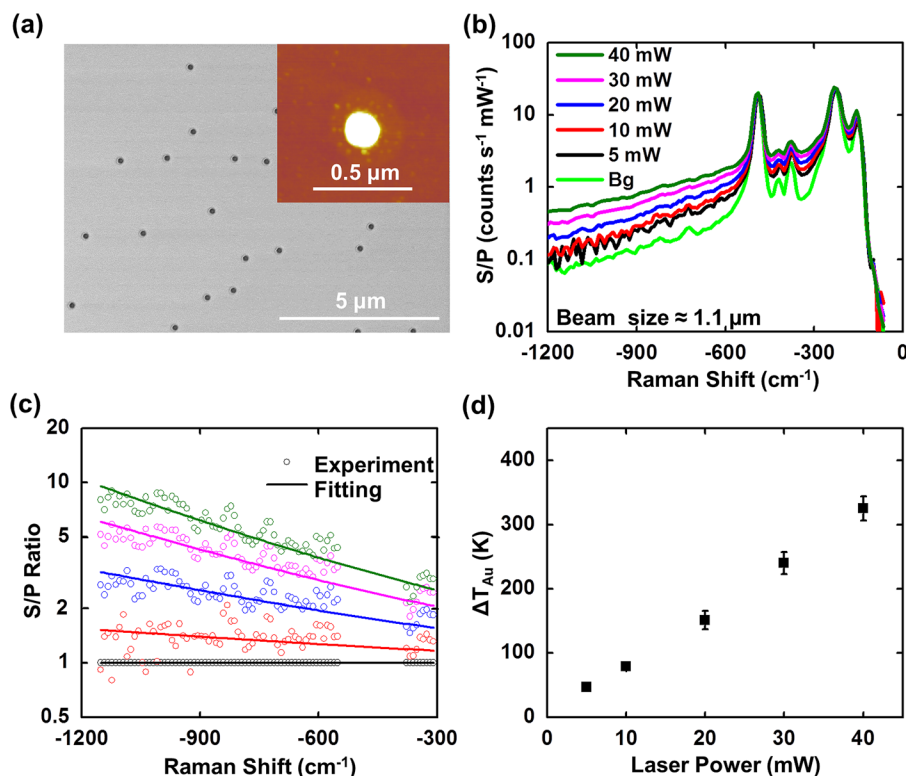


FIG. 2. Raman spectra and temperature measurement for an individual plasmonic nanodisk. (a) The SEM image of widely-dispersed individual plasmonic nanodisks on the quartz substrate. The inset shows the atomic force microscopy (AFM) image of an individual nanodisk. (b) Raman spectra for a representative nanodisk under laser illumination as a function of laser power. The green line is the background spectrum for quartz collected at an area adjacent to the nanodisk. (c) Data and fits for the Raman spectra normalized by the spectrum collected at a laser power of 5 mW. (d) The temperature of the nanodisk extracted from fits to Eq. (2) as a function of laser power.

self-consistent result using an iterative approach. The iteration begins by setting the value of T_0 as room temperature (denoted as T_{RT}) and fitting the data to extract T_{Au} at different laser power P . We then extrapolate T_{Au} to $P=0$ mW (denoted as T_I) and start a new iteration by adjusting T_0 to minimize the absolute value of $T_I - T_{RT}$. The iteration ends when $|T_I - T_{RT}| < 0.5$ K.

Figure 2(d) shows the resulting temperature rise (i.e., $T_{Au} - T_{RT}$) for the individual Au nanodisk as a function of laser power. For a power of 5 mW, the temperature rise is ≈ 45 K. We find that typical experimental uncertainties in the temperature measurement are $\approx 3\%$ of the absolute temperature. The high sensitivity of $\frac{S(\Delta\omega)_{Au}}{S(\Delta\omega)_0}$ to T_{Au} (Fig. S4) helps to reduce the propagation of spectral noise to the uncertainty of the extracted temperature. Thereby, the uncertainty from fitting the spectra of individual nanodisk is only slightly larger than that from fitting the spectra of nanodisk arrays.

To assess the effectiveness of using anti-Stokes electronic Raman scattering for evaluating the temperature of individual nanodisks, we calculated the expected temperature excursion and compared with experiment. The diameter (D), absorption cross-section (σ_{abs}) of the Au nanodisk, thermal conductivity of the quartz substrate (Λ), interfacial thermal conductance (G_{int}) between the nanodisk and quartz are determined in separate experiments. Details of these measurements are included in the [supplementary material](#).

Figure 3(a) shows the measured average absorption cross-section (σ_{abs}) for an ensemble of Au nanodisks. The measurement uses an UV-vis-NIR spectrometer with an integrating sphere detector.³⁸ The areal density of nanodisks is determined by SEM; $\sigma_{abs} \approx 0.024 \mu\text{m}^2$ near resonance, comparable to the physical area of the nanodisk, and approximately 20% of the extinction cross-section σ_{ext} . We use time-domain-thermoreflectance (TDTR)^{39–41} to measure Λ by fitting a thermal model

with Λ as the only free parameter to the measured TDTR signals. We treat the ST-cut quartz (angle $42^\circ 45'$) as isotropic, obtaining $\Lambda = 7.9 \pm 0.70 \text{ W m}^{-1} \text{ K}^{-1}$ (Fig. S7 in the [supplementary material](#)) that is consistent with the literature reported values ($6.9 \text{ W m}^{-1} \text{ K}^{-1}$ and $11 \text{ W m}^{-1} \text{ K}^{-1}$ for two principal directions, respectively).⁴²

For thermal transport on nanometer length scales, the thermal conductance of interfaces (G_{int}) plays a key role but has often been ignored in prior studies of the heating of plasmonic nanostructures. We use time-domain-transient-attenuation (TDTA) to measure G_{int} for the nanodisk/substrate interface.^{43,44} TDTA detects the transient change of optical extinction of the plasmonic nanodisks (circles in Fig. 3(b)) when heated by laser pulses. We fit the data to a thermal transport model and find $G_{int} = 100 \pm 20 \text{ MW m}^{-2} \text{ K}^{-1}$ (Fig. 3(b) and Fig. S8 in the [supplementary material](#)). Because the Kaptiza length, $L_K = \Lambda / G_{int} = 80 \text{ nm}$, is much larger than the thickness of the Au nanodisk ($h = 23 \text{ nm}$), the temperature decay of the nanodisk following pulsed ps heating is approximately exponential with a thermal time constant $hC_{Au} / G_{int} = 570 \text{ ps}$, where $C_{Au} = 2.46 \text{ J cm}^{-3} \text{ K}^{-1}$ is the heat capacity of Au.

The temperature rise of the Au nanodisk can be calculated analytically as

$$\theta_{Au} = \frac{f_i \pi D}{\sigma_{phy} \Lambda} \int_0^{D/2} r \int_0^\infty \frac{J_0(kr) J_1(kD/2)}{k} dk dr + f_i / G_{int} \quad (3)$$

where $f_i = \frac{2P}{\pi W_0^2} H(\frac{D}{2} - r) \frac{\sigma_{abs}}{\sigma_{phy}}$ is the heat flux, P is the power of the laser beam, W_0 is the $1/e^2$ radius, $H(D/2 - r)$ is a Heaviside function, D is the diameter of the nanodisk, $\sigma_{phy} = \pi D^2 / 4$ is the physical cross-section, and J_0 and J_1 are the zero and first order Bessel function, respectively. Details of the calculation appear in the [supplementary material](#).

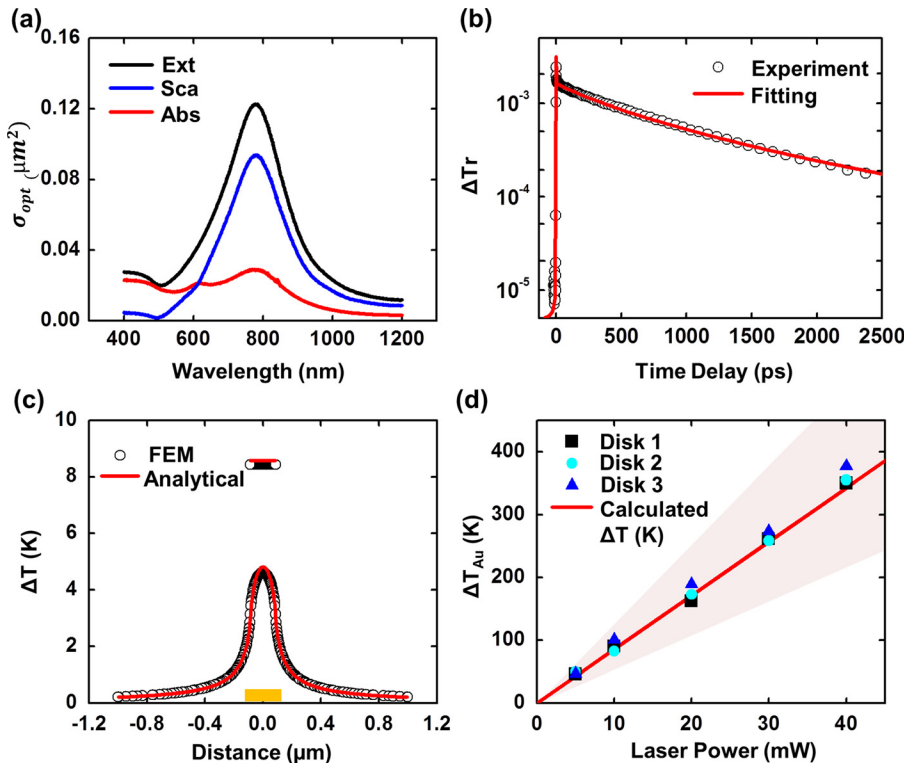


FIG. 3. Calculation of the temperature excursion for an individual plasmonic nanodisk and comparison with experiment. (a) Measured average extinction (Ext), scattering (Sca), and absorption (Abs) cross-sections for an Au nanodisk. The measurements use an ensemble of nanodisks with diameter $174 \text{ nm} \pm 20 \text{ nm}$. (b) Time-domain transient attenuation (TDTA) data (black circle) of nanodisks and corresponding fit (red line) to a heat diffusion model. The extracted interfacial thermal conductance between the Au nanodisk and quartz substrate is $100 \pm 20 \text{ MW m}^{-2} \text{ K}^{-1}$. (c) Finite element modeling (FEM, black circle) and analytical calculation (red line) of the temperature excursion for an nanodisk with an incidence laser power of 1 mW focused to a $1/e^2$ intensity radius of $1.1 \mu\text{m}$. (d) Comparison between the temperature rise measured by electronic Raman scattering (black squares, cyan dots and blue triangles) to the calculation (red line) as a function of laser power. The shaded region corresponds to the uncertainties of the calculation.

Figure 3(c) shows the calculated temperature rise for the Au nanodisk and the surface of the quartz substrate at a laser power of 1 mW. Finite-element modeling (FEM, circles) and the analytical solution of the heat conduction (solid lines) yield similar results. The temperature rise in the nanodisk is uniform due to the high thermal conductivity of Au. We find a large temperature drop between the nanodisk and the quartz surface due to the fact that the Kapitza length for the interfacial conductance is comparable to the radius of the nanodisk. The ratio of the temperature drop at the interface to the temperature drop in the substrate is ≈ 1.2 .

Finally, we compare the calculated temperature rise to the temperature excursion measured by the electronic Raman scattering spectra in Fig. 3(d). Temperature excursions measured on three nanodisks are plotted as a function of laser power (solid symbols). The calculation (red line) and overall uncertainties (shaded region) originated from error propagation in each parameter (Table S1 in [supplementary material](#)) are in good agreement with the data.

In conclusion, we show that anti-Stokes electronic Raman scattering provides a non-invasive, accurate method to determine the temperature of plasmonic structures in real-time operation. The upper temperature of our experiments of 650 K is limited by the thermal stability of the Au nanodisks we studied and is not a fundamental limit of the approach. The thermometry is applicable to arrays of nanodisks with a spatial resolution set by the diffraction limit of probing laser, and a temperature accuracy of 2%. When applied to individual nanodisks of sub-100 nm radius, the thermometry has a slightly lower accuracy of 3% due to variations in the baseline spectrum. A reduction in background fluorescence from the substrate and optical elements could increase the accuracy. The experimental and analysis framework presented here provide useful tools for monitoring the temperature of metallic nanostructures in thermoplasmonics² such as chemical catalysts and HAMR technology.

See [supplementary material](#) for details of the fabrication of Au plasmonic nanodisks, measurement of the electronic Raman scattering, and calculation of the temperature rise for individual plasmonic nanodisk.

We thank Dr. Jingyu Huang and Dr. Jonglo Park for helpful discussions on Raman spectroscopy and transient absorption measurements, respectively. We thank Hyejin Jiang for the assistance on measurements of laser spot sizes. We thank Dr. Patrick Fletcher and Dr. Xuan Zheng for helpful discussions on HAMR and our experimental results. The sample preparation and measurement were carried out in part in the Frederick Seitz Materials Research Laboratory Central Research Facilities, University of Illinois at Urbana-Champaign. We acknowledge the funding supported by Seagate Technology.

¹J. A. Schuller, E. S. Barnard, W. S. Cai, Y. C. Jun, J. S. White, and M. L. Brongersma, *Nat. Mater.* **9**, 193 (2010).

²G. Baffou and R. Quidant, *Laser Photonics Rev.* **7**, 171 (2013).

³M. I. Stockman, *Science* **348**, 287 (2015).

⁴E. M. Larsson, C. Langhammer, I. Zoric, and B. Kasemo, *Science* **326**, 1091 (2009).

⁵T. Vo-Dinh, H.-N. Wang, and J. Scaffidi, *J. Biophotonics* **3**, 89 (2010).

⁶A. G. Brolo, *Nat. Photonics* **6**, 709 (2012).

⁷Z. P. Qin and J. C. Bischof, *Chem. Soc. Rev.* **41**, 1191 (2012).

⁸X. H. Huang, P. K. Jain, I. H. El-Sayed, and M. A. El-Sayed, *Laser Med. Sci.* **23**, 217 (2008).

⁹M. A. Green and S. Pillai, *Nat. Photonics* **6**, 130 (2012).

¹⁰M. L. Brongersma, N. J. Halas, and P. Nordlander, *Nat. Nanotechnol.* **10**, 25 (2015).

¹¹W. A. Challener, C. B. Peng, A. V. Itagi, D. Karns, W. Peng, Y. G. Peng, X. M. Yang, X. B. Zhu, N. J. Gokemeijer, Y. T. Hsia, G. Ju, R. E. Rottmayer, M. A. Seigler, and E. C. Gage, *Nat. Photonics* **3**, 303 (2009).

¹²L. Shi, C. Dames, J. R. Lukes, P. Reddy, J. Duda, D. G. Cahill, J. Lee, A. Marconnet, K. E. Goodson, J. H. Bahk, A. Shakouri, R. S. Prasher, J. Felts, W. P. King, B. Han, and J. C. Bischof, *Nanoscale Microscale Thermophys. Eng.* **19**, 127 (2015).

¹³G. P. Ju, Y. G. Peng, E. K. C. Chang, Y. F. Ding, A. Q. Wu, X. B. Zhu, Y. Kubota, T. J. Klemmer, H. Amini, L. Gao, Z. H. Fan, T. Rausch, P. Subedi, M. J. Ma, S. Kalarickal, C. J. Rea, D. V. Dimitrov, P. W. Huang, K. K. Wang, X. Chen, C. B. Peng, W. B. Chen, J. W. Dykes, M. A. Seigler, E. C. Gage, R. Chantrell, and J. U. Thiele, *IEEE Trans. Magn.* **51**, 3201709 (2015).

¹⁴ASTC Technology Roadmap (2016).

¹⁵T. Rausch, E. Gage, and J. Dykes, *Ultrafast Magn.* **1** 159, 200 (2015).

¹⁶W. Jeong, S. Hur, E. Meyhofer, and P. Reddy, *Nanoscale Microscale Thermophys. Eng.* **19**, 279 (2015).

¹⁷X. Xie, K. L. Grosse, J. Song, C. Lu, S. Dunham, F. Du, A. E. Islam, Y. Li, Y. Zhang, E. Pop, Y. Huang, W. P. King, and J. A. Rogers, *ACS Nano* **6**, 10267 (2012).

¹⁸G. Baffou, P. Bon, J. Savatier, J. Polleux, M. Zhu, M. Merlin, H. Rigneault, and S. Monneret, *ACS Nano* **6**, 2452 (2012).

¹⁹M. Siler, J. Jezek, P. Jakl, Z. Pilat, and P. Zemanek, *Opt. Lett.* **41**, 870 (2016).

²⁰Z. J. Coppens, W. Li, D. G. Walker, and J. G. Valentine, *Nano Lett.* **13**, 1023 (2013).

²¹G. Baffou, M. P. Kreuzer, F. Kulzer, and R. Quidant, *Opt. Express* **17**, 3291 (2009).

²²L. Li, B. Suen, and F. E. Talke, *IEEE Trans. Magn.* **51**, 3301204 (2015).

²³Y. Yue and X. Wang, *Nano Rev.* **3**, 11586 (2012).

²⁴H. K. Lyoo and D. G. Cahill, *Phys. Rev. B* **73**, 144301 (2006).

²⁵M. R. Beversluis, A. Bouhelier, and L. Novotny, *Phys. Rev. B* **68**, 115433 (2003).

²⁶J. Y. Huang, W. Wang, C. J. Murphy, and D. G. Cahill, *Proc. Natl. Acad. Sci. U. S. A.* **111**, 906 (2014).

²⁷J. T. Hugall and J. J. Baumberg, *Nano Lett.* **15**, 2600 (2015).

²⁸M. Bayle, N. Combe, N. M. Sangeetha, G. Viau, and R. Carles, *Nanoscale* **6**, 9157 (2014).

²⁹M. Bayle, P. Benzo, N. Combe, C. Gatel, C. Bonafos, G. Benassayag, and R. Carles, *Phys. Rev. B* **89**, 195402 (2014).

³⁰R. Carles, M. Bayle, P. Benzo, G. Benassayag, C. Bonafos, G. Cacciato, and V. Privitera, *Phys. Rev. B* **92**, 174302 (2015).

³¹H. Fredriksson, Y. Alaverdyan, A. Dmitriev, C. Langhammer, D. S. Sutherland, M. Zaeck, and B. Kasemo, *Adv. Mater.* **19**, 4297 (2007).

³²I. Zoric, M. Zach, B. Kasemo, and C. Langhammer, *ACS Nano* **5**, 2535 (2011).

³³C. Langhammer, M. Schwind, B. Kasemo, and I. Zoric, *Nano Lett.* **8**, 1461 (2008).

³⁴R. S. Krishnan, *Nature* **155**, 452 (1945).

³⁵M. V. Klein, in *Theory of Light Scattering in Condensed Matter*, edited by B. Bendow, J. L. Birman, and V. M. Agranovich (Springer, Boston, 1976), p. 461.

³⁶B. Liu, Z. H. Yu, Z. P. Tian, D. Homa, C. Hill, A. Wang, and G. Pickrell, *Opt. Lett.* **40**, 2041 (2015).

³⁷X. J. Wang, C. D. Liman, N. D. Treat, M. L. Chabinyc, and D. G. Cahill, *Phys. Rev. B* **88**, 075310 (2013).

³⁸C. Langhammer, B. Kasemo, and I. Zoric, *J. Chem. Phys.* **126**, 194702 (2007).

³⁹D. G. Cahill, *Rev. Sci. Instrum.* **75**, 5119 (2004).

⁴⁰A. J. Schmidt, X. Y. Chen, and G. Chen, *Rev. Sci. Instrum.* **79**, 114902 (2008).

⁴¹X. Xie, D. Y. Li, T. H. Tsai, J. Liu, P. V. Braun, and D. G. Cahill, *Macromolecules* **49**, 972 (2016).

⁴²J. P. Feser, J. Liu, and D. G. Cahill, *Rev. Sci. Instrum.* **85**, 104903 (2014).

⁴³J. Park, J. Y. Huang, W. Wang, C. J. Murphy, and D. G. Cahill, *J. Phys. Chem. C* **116**, 26335 (2012).

⁴⁴J. Park and D. G. Cahill, *J. Phys. Chem. C* **120**, 2814 (2016).